Railway Engineering Science
https://doi.org/10.1007/s40534-024-00372-2

Experimental study to evaluate the impact of bubble defects on the interfacial bonding properties of the self-compacting concrete filling layer

Wei Jiang[1] · Youjun Xie[2] · Yi-Qing Ni[3] · Su-Mei Wang[3] · Qiang Fu[4] · He Liu[5] · Ning Li[6] · Wenxu Li[7] · Guangcheng Long[2]

Received: 9 September 2024 / Revised: 12 December 2024 / Accepted: 14 December 2024

Abstract
The current technical standards primarily relied on experience to judge the interfacial bonding properties between the self-compacting concrete filling layer and the steam-cured concrete precast slab in CRTS III slab ballastless track structure. This study sought to enhance technical standards for evaluating interfacial bonding properties by suggesting the use of the splitting tensile strength to evaluate the impact of bubble defects. Specimens were fabricated through on-site experiment. The percent of each area of 6 cm^2 or more bubble defect was 0 in most of specimens. When the cumulative area of all bubble defects reached 12%, the splitting tensile strength value was 0.67 MPa, which exceeded the minimum required value of 0.5 MPa for ensuring bonding interface adhesion. Furthermore, when the cumulative area of all bubble defects reached 8%, the splitting tensile strength value was 0.85 MPa, which exceeded the minimum required value of 0.8 MPa, thereby overcoming the negative impact of each area of 10 cm^2 or more bubble defect. Additionally, keeping the cumulative area of each area of 6 cm^2 or more bubble defect below 6% ensured adequate bonding strength and reduced the occurrence of specimens with lower splitting tensile strength values.

Keywords CRTS III slab ballastless track structure · Self-compacting concrete · Bubble defect · Interfacial bonding property · Splitting tensile strength

1 Introduction

The CRTS III slab ballastless track structure was a ballastless track structure designed and constructed by China. At present, the operating mileage of this advanced track structure in China had exceeded 9000 km. Meanwhile, the Jakarta-Bandung High-Speed Railway, constructed using this advanced track structure and connecting Jakarta and Bandung in Indonesia, officially began commercial operation on October 2, 2023. This advanced track structure ensured safe, comfortable, and efficient operation of high-speed trains at a speed of 350 km/h, greatly changing the way residents travel. This advanced track structure was including the steam-cured concrete precast slab (the precast slab), the self-compacting concrete filling layer (the filling layer), the geotextile layer, and the base plate. The precast slab was manufactured in the factory, with each standard precast slab measuring 5600 mm in length, 2500 mm in width, and 200 mm in depth. At the site, the filling layer was subsequently perfused to achieve standard dimensions

✉ Guangcheng Long
longguangcheng@csu.edu.cn

Wei Jiang
railwaywilliam@163.com

1 School of Infrastructure Engineering, Nanchang University, Nanchang 330031, China

2 School of Civil Engineering, Central South University, Changsha 410075, China

3 Department of Civil and Environmental Engineering, The Hong Kong Polytechnic University, Hung Hom, Kowloon, Hong Kong SAR

4 College of Civil Engineering, Xi'an University of Architecture & Technology, Xi'an 710055, China

5 School of Transportation and Geomatics Engineering, Shenyang Jian Zhu University, Shenyang 110168, China

6 School of Civil Engineering, Qingdao University of Technology, Qingdao 266033, China

7 School of Civil Engineering, Jiangsu University of Science and Technology, Jiangsu 212100, China

Published online: 05 February 2025

of 5600 mm in length, 2500 mm in width, and 90 mm in depth. Figure 1 shows the condition of this track structure after completion of construction.

The filling layer mainly played the roles of the supporting, adjusting, and bonding. This track structure required the filling layer to form a composite plate structure with the precast slab [1]. Through the perfusion hole in Fig. 1, the filling layer was created by on-site filling of the self-compacting concrete (SCC) in the nearly sealed space. The process of filling self-compacting concrete on-site was a complex process and also required very careful handling. Initially, a white polyvinyl chloride (PVC) pipe, typically with a diameter of 18.0 cm, slightly smaller than the perfusion hole for a secure fit, was installed at the perfusion hole of the precast slab. The PVC pipe usually extended 1.0 m above the precast slab. It was through this pipe that the SCC was introduced into the nearly sealed space. During the on-site filling of the SCC, four pulping outlets of the precast slab were opened, enabling the SCC to gradually displace the air from the nearly sealed space and fill it. Simultaneously, a portion of the SCC slowly flowed out into the external space through these outlets. When an overflow of SCC was observed from the top of the PVC pipe, the four pulping outlets were swiftly closed to prevent further outflow. Thus, the entire perfusion process was completed. This process could take anywhere from 6 to 10 min, depending on the raw materials used in the SCC. Notably, the grading of the coarse aggregate had a significant impact on the duration of the perfusion process. Therefore, several filling experiments would be conducted beforehand at the construction site to establish an appropriate filling rate and time. The field perfusion process of the SCC is depicted in Fig. 2.

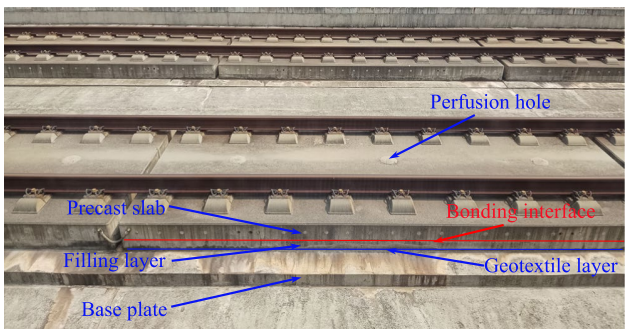

Fig. 1 The condition of this track structure after completion of construction

The SCC was a mixture of different solid, liquid, and gas polyphases that were highly sensitive [2–6]. In particular, the approximate sealed space in Fig. 2 was used for on-site filling. This construction method made it possible for segregation to occur in the SCC. If segregation of the SCC occurred during the perfusion process, then the bonding performance would be seriously affected. This had serious implications for the durability. Therefore, it was very necessary to check the quality of the bonding interface.

Because the CRTS III slab ballastless track structure was a new type of track structure, there may be some problems in the current construction process. According to the current Chinese technical standards [7], if the construction unit filled 2000 precast slabs or if there was any doubt regarding the quality of the filling layer, it was required to uncover precast slabs on-site for inspection. This inspection should include taking at least one precast slab to assess the perfusion quality. The apparent morphology of two standard-sized filling layers obtained through on-site uncovering plate method was selected, as shown in Fig. 3.

To carry out a quantitative assessment of bonding interface defects, it was imperative to guarantee that the surface of the filling layer was devoid of any bubbles exceeding 50 cm^2 in size, and that the total cumulative area occupied by bubbles measuring 6 cm^2 or more did not surpass 2% [8]. The quality of perfusion was assessed primarily by the area occupied by interfacial bubble defects, a determination heavily reliant on field experience.

The assessment of bonding performance between the filling layer and the precast slab continued to hinge on

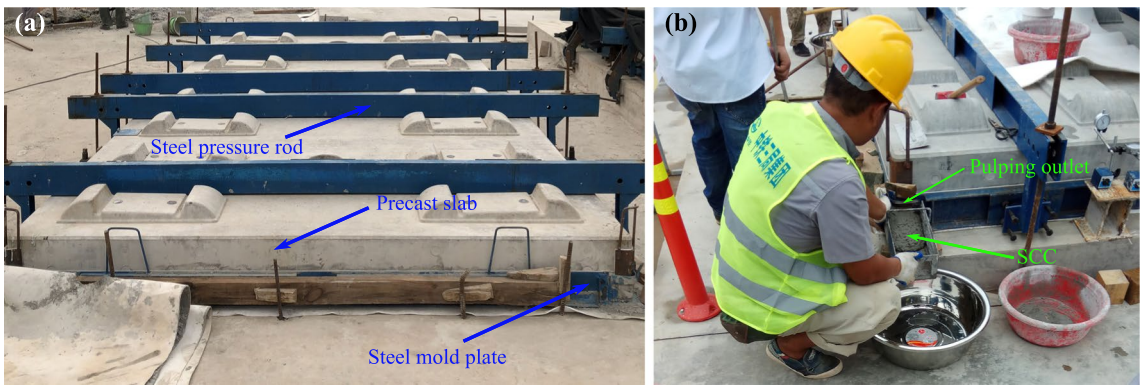

Fig. 2 The field perfusion process: **a** the nearly sealed space; **b** the SCC flowing out of the pulping outlet

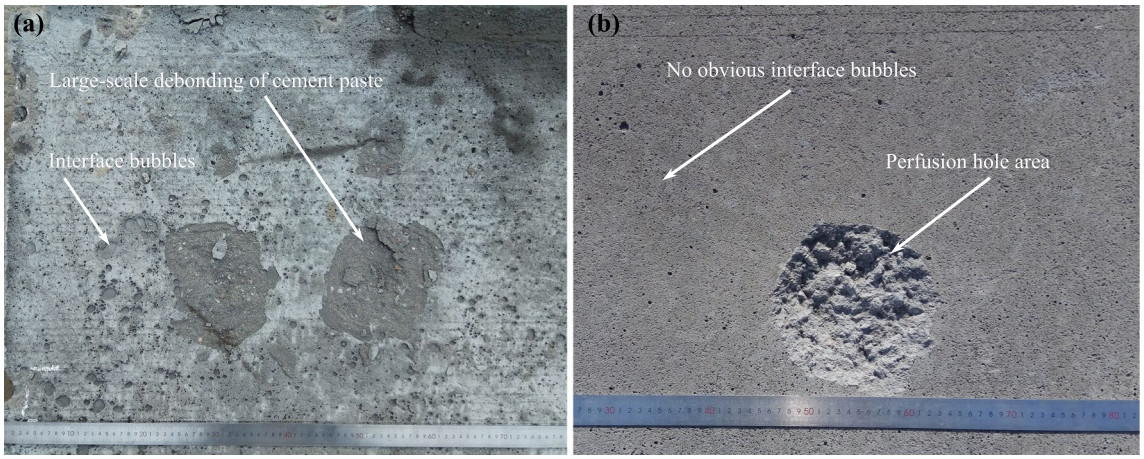

Fig. 3 Apparent morphology: **a** obvious interface defects; **b** no obvious interface defects

experience, lacking a scientific basis for judgment. To enhance the existing technical standards in China [7, 8], the authors proposed that adopting a mechanical indicator for evaluation, through on-site experimentation, could be a more suitable approach.

The SCC was the concrete material with complex and diverse components. To ensure excellent flowability and self-compacting properties, the SCC composition included various components. Many scholars studied the effect of aggregate composition [9–11], asphalt admixture [12, 13], nanoadditives [14–16], activated powder admixture [17], rubber admixture [18–21], and fiber admixture [22–25] on the properties of the SCC. Changes in the properties of the SCC by the addition of specific materials, such as the pumice [26], polyvinyl alcohol [27], glass [28], limestone [29, 30], and steel fibers [31–39], were also studied. Scholars studied the effect of the presence of admixtures [40], geopolymers [41, 42], and plasticizers [43, 44] on the properties of the SCC. The process of the SCC from the beginning of mixing to pouring and molding was also influenced by many factors. Scholars studied cement hydration [45], temperature [46, 47], shrinkage [48, 49], rheology [50–53], surface damage [54], and self-healing [55] in the SCC. As for the establishment of mechanical evaluation methods, scholars carried out studies on numerical simulation [56, 57], reinforcement bonding [58–64], and interface bonding [65, 66]. The size and distribution of bubbles, the design of the concrete mix, curing conditions, fiber reinforcement, concrete handling, and construction practices could all exert a significant influence on bubble defects. This paper focused on railway-specific SCC. The presence of interface defects could impair the bonding performance between the filling layer and the precast slab, particularly under repeated dynamic loads from high-speed trains traveling at speeds up to 350 km/h. This would expedite the infiltration of external moisture, causing initial interface defects to expand, impacting the dynamic performance of the track structure, and altering the structural dynamics of the joint work between the filling layer and the precast slab. This type of concrete had specific compositional requirements [8]. According to the current Chinese technical standards [67], it may be a more effective way to evaluate bubble defects by using the mechanical indicator. Analyzed the correlation between bubble defects and splitting tensile strength, the use of the splitting tensile strength to evaluate the impact of bubble defects on the interfacial bonding properties was of practical engineering interest.

2 Experimental setup

Considering the length and width of each standard precast slab shown in Fig. 1, as well as the dense multilayered thick reinforcement inside, it was difficult to accomplish the splitting tensile strength experiment on standard precast slab directly. In order to change this difficult situation, the authors created small-size experimental slabs at the same fabrication factory. These experimental slabs measured 2400 mm in length and 400 mm in width. As per the on-site infusion experiment, each experimental slab was filled with the SCC on-site, as illustrated in Fig. 4. A total of eight small-size experimental slabs underwent field infusion experiments. These experimental slabs were filled with SCC and then subjected to daily maintenance.

The composition of the SCC used for small-size experimental slabs is presented in Table 1.

The raw materials in Table 1 were the raw materials used in the section where the on-site experiment was conducted. The manufacturer of the cement was Fenyi Hailuo Cement Limited Liability Company, and the cement was low-alkali cement with P·O 42.5. The manufacturer of the coarse aggregate was Jishui County Badu Songjia Quarry, and the grading was a continuous-type grading from 5 to 16 mm. The river sand was

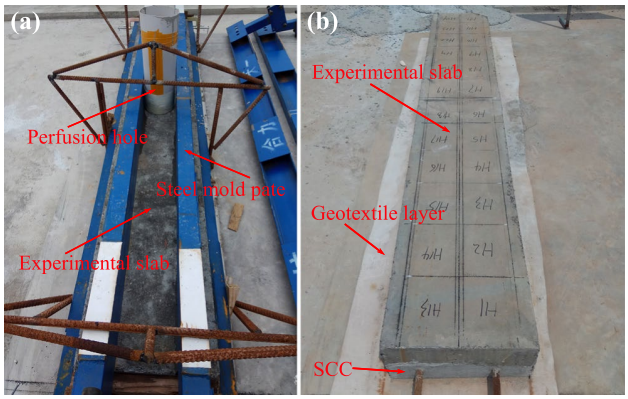

Fig. 4 Each experimental slab: **a** before the start of the perfusion experiment; **b** after completion of the perfusion experiment

Ganjiang sand, which was graded as medium-sized sand. The water was mainly groundwater used. The manufacturer of the fly ash was Jiangsu Mingjiang Engineering Company, and the grade was C50 and above. The manufacturer of the ground blast furnace slag was Jiangxi Xinyu South Building Materials Company, and the grade was S95. The manufacturer of the expansion admixture was Shanxi Zhongtie Tiecheng Building Material Technology Company, and the grade was ZT-5. The manufacturer of the viscosity-modified admixture was Beijing Tieke Shougang Railway Technology Company, and the grade was TK-M. The manufacturer of the water reducer was Sichuan Hengze Building Material Company, and the grade was HZ-01 polycarboxylic acid (Standard). Indeed, during the actual construction of high-speed railways, the entire route was divided into numerous sections to facilitate simultaneous construction, with each section spanning approximately 20–30 km. Within the same section, the raw materials utilized on-site remain largely consistent. Nevertheless, there may be variations in the raw materials employed across different sections. Even in cases where different sections utilized differing raw materials, the on-site construction team performed extensive experiments prior to pouring self-compacting concrete to guarantee compliance with national standards.

Regarding the field test results for freshly mixed SCC, the slump flow measured 670 mm, the slump-flow time was 5 s, the J-ring blocking step was 14 mm, the L-box filling ratio was 0.9, there was no water secretion, the air content was 4.5%, and the vertical expansion ratio was 0.2%. As for the hardened SCC performance parameters, the compressive strength was 22.2 MPa at 3 days, 31.8 MPa at 7 days, and 43.6 MPa at 28 days. The flexural strength at 56 days was 6.9 MPa.

Once daily maintenance of each experimental slab was finished, these slabs were transported to the cutting plant to undergo the cutting process, as illustrated in Fig. 5. During the cutting process, the cutting machine should try to cut as slowly and evenly as possible to reduce the effect of vibration on these experimental slabs.

The slab in Fig. 5 was cut into small specimens following the labeled lines in Fig. 4b. In this way each small-size experimental slab could be cut into a maximum of 24 small specimens. After all small-size experimental slabs were cut, the small specimens obtained were transported back for the splitting tensile strength experiment [67]. Figure 6 shows a schematic diagram of this experiment. Upon activating the testing machine, the surface of the concrete specimen and the cushion strip should make uniform contact. The load should be applied in a continuous and uniform manner throughout the test. Given that the strength class of the SCC was C40 and that of the experimental slab was C60, the loading speed should be set at 0.08 MPa/s. If the manual method was used to control the loading speed of the press, when the concrete specimen was close to destruction, it should be stopped to adjust the throttle of the testing machine until destruction and then record the destruction load.

Fig. 5 The cutting process of each experimental slab

Table 1 The composition of the SCC used for the on-site perfusion experiment (unit: kg/m^3)

Cement	Coarse aggregate		River sand	Water	Fly ash	Ground blast furnace slag	Expansion admixture	Viscosity-modified admixture	Water reducer
	5–10 mm	10–16 mm							
300	318	477	860	175	90	66	50	24	5.4

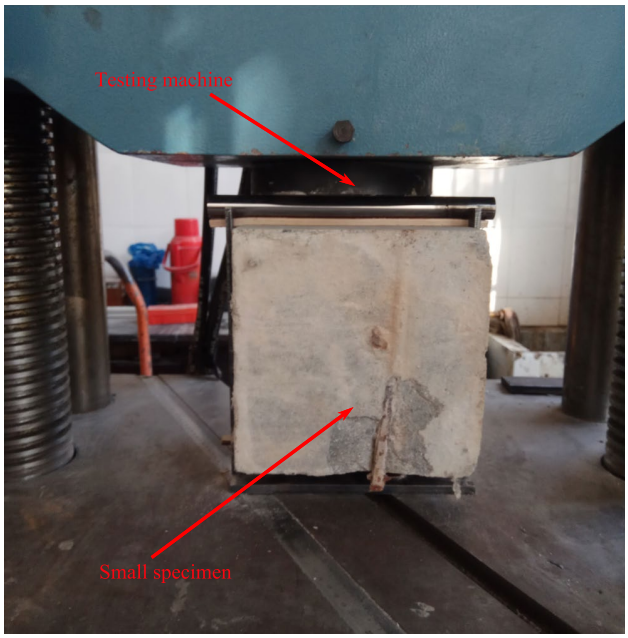

Fig. 6 Splitting tensile strength experiment

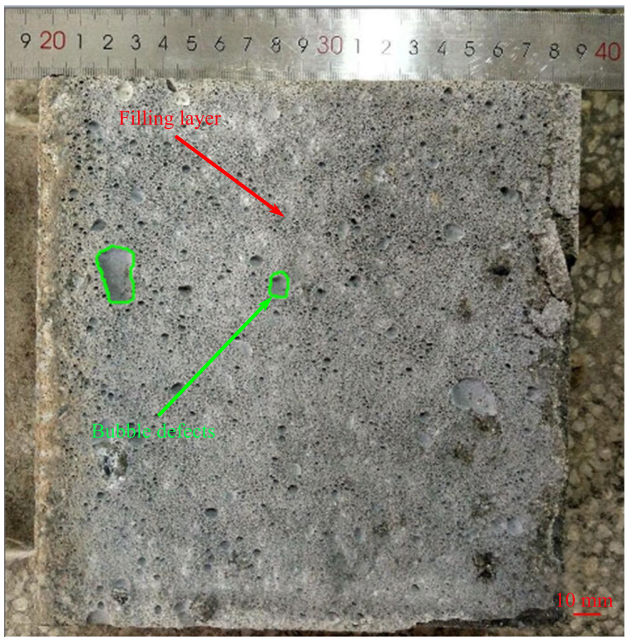

Fig. 7 Schematic diagram for counting the area of bubble defects

The concrete splitting tensile strength of each specimen in Fig. 6 should be calculated according to Eq. (1) [67]:

$$f_{ts} = \frac{2F}{\pi A}, \tag{1}$$

where f_{ts} was concrete splitting tensile strength (MPa), F was specimen destructive load (N), and A was specimen splitting surface area (mm^2).

The splitting tensile strength value for each specimen could be obtained through the experiment. These papers mentioned the use of more refined wedge-splitting test to obtain splitting tensile strength [68, 69]. Also, the apparent morphology could be obtained. The area of defect per bubble was counted using the Image-Pro software, as shown in Fig. 7.

As many bubble defects on the surface of the filling layer as possible were counted for subsequent analysis according to the method in Fig. 7.

3 Results and discussion

The current Chinese technical standards mentioned the impact of two types of bubble defects, that were, no contain any bubbles larger than 50 cm^2 and total cumulative area of bubbles measuring 6 cm^2 or more should not exceed 2% [8]. Based on the field experiment described above, the relationship between the splitting tensile strength value and the percent of the sum of each area of 6 cm^2 or more bubble defect is shown in Fig. 8.

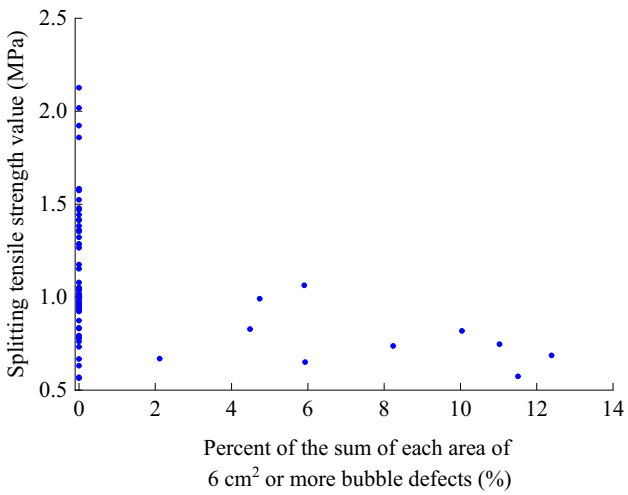

Fig. 8 The relationship between the strength value and the percent of the sum of each area of 6 cm^2 or more bubble defects

As illustrated in Fig. 8, for the majority of the specimens, the percentage of the total area occupied by bubble defects, each with an area of 6 cm^2 or more, relative to the entire filling layer, was zero. Conversely, in a minority of specimens, this percentage exceeded 2%, and in some cases, it was remarkably high, surpassing even 12%. The horizontal axis in Fig. 8 featured a substantial number of zero-value points, signifying that these specimens contained no bubble defects with an area of 6 cm^2 or more. Notably, the distribution of splitting tensile strength

values along the vertical axis exhibited considerable variability among these specimens. This significant variation could primarily be attributed to the differing distributions of much smaller bubble defects, specifically those with individual areas less than 6 cm^2, throughout the concrete specimens. This explained the high degree of variability observed in the interfacial bubble defects within each specimen.

On the one hand, the current Chinese technical standards do not directly address interfacial bonding performance. Conversely, comprehensive on-site uncovering tests revealed a substantial number of single bubble defects on the surface, each measuring less than or slightly below 6 cm^2. These bubble defects were highly likely to accumulate and constitute more than 2% of the filling layer area. To meticulously analyze the relationship between different types of bubble defects and interfacial bonding performance, two standard-sized filling layers were selected based on the field uncovering method. A camera was employed to capture images of the bonding interface in sections, which were subsequently pieced together to form a complete view of the entire bonding interface. Two standard-sized filling layers are visually represented in Fig. 9.

An area captured by the camera was chosen for comparative analysis, and Fig. 10 depicts the interfacial bubble defects present in the observation hole area of these two standard-sized filling layers. The area shown in Fig. 10 was a partial area in Fig. 9. The two regions in Fig. 10 corresponded to the same positions of two standard-sized filling layers in Fig. 9. The length and width of the area shown in Fig. 10 were 900 and 630 mm, respectively.

As depicted in Fig. 10a, the first plate exhibited no significant bubble defects, primarily featuring bubble defects of smaller areas. In contrast, Fig. 10b shows that the second plate had noticeable bubble defects. Employing the method outlined in Fig. 7, the areas of the bubble defects in these two standard-sized filling layers were calculated. To enhance accuracy, the bubble defect area was categorized into three ranges: (10 mm^2, 100 mm^2), [100 mm^2, 600 mm^2), and [600 mm^2, ∞) for statistical analysis. The results of this analysis are presented in Table 2.

By examining Table 2, it was evident that within the range of individual bubble defect area (10 mm^2, 100 mm^2), there was minimal disparity in the percent of the cumulative bubble defect areas for each category to the filling layer. However, in the classification interval where the area of individual bubble defects exceeded 100 mm^2, the percent of the cumulative areas for each type of bubble defect to the filling layer exhibited significant variations. Notably, when large bubble defect emerged at the interlayer interface, the percent of the cumulative areas of these bubble defects to the filling layer increased noticeably. Hence, all specimens with large

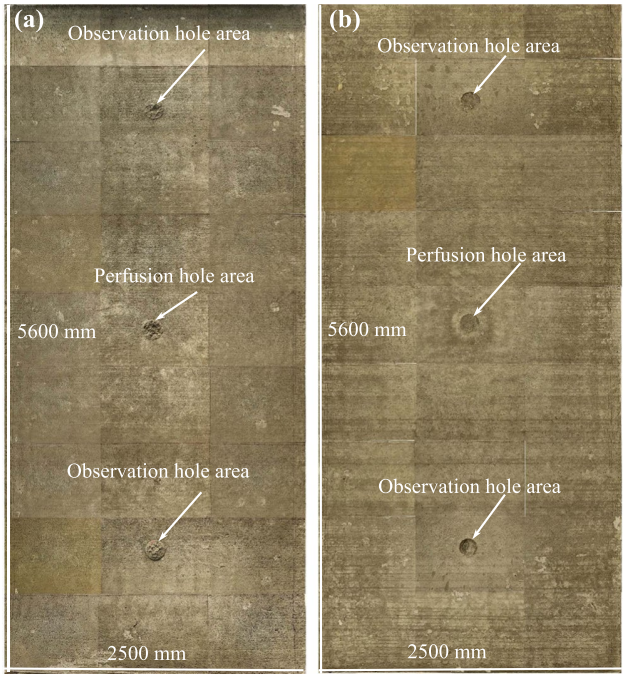

Fig. 9 Surface of two standard-sized filling layers: **a** the first plate; **b** the second plate

bubble defect greater than 100 mm^2 were categorized. The classification is presented in Table 3.

Bubble defects of all specimens were divided into 10 categories in Table 3, and s represented the single bubble defect area. According to the cutting method in Fig. 5, the cross-sectional size of the interlayer interface for each specimen was approximately 200 mm × 200 mm. The correlation between the classification of bubble defects, the percentage of the cumulative bubble defect area, and the relative rate of decrease in the splitting tensile strength value was examined, as depicted in Fig. 11.

This analysis offered a comprehensive overview of the distribution of bubble defects across various ranges of the bonding interface. It was clear that the percentage of bubble defects increased as the range increased, with the highest percentage found in the range of 1000 $mm^2 \le s$. However, it was also noted that there were no specimens with bubble defects within certain ranges, such as 600 $mm^2 \le s < 700$ mm^2, 800 $mm^2 \le s < 900$ mm^2, and 900 $mm^2 \le s < 1000$ mm^2. This observation may indicate that the formation of bubble defects was not consistent across the bonding interface. Additionally, the emphasis on the presence of bubble defects at the interlayer interface suggested a potential impact on the performance and reliability of this structure. From the comparison of Fig. 11a–j, it could be observed that the trend of each area of 100 mm^2 or more bubble defect was that the probability of occurrence decreased as single bubble defect increased. Regarding bubble defects with a single defect area

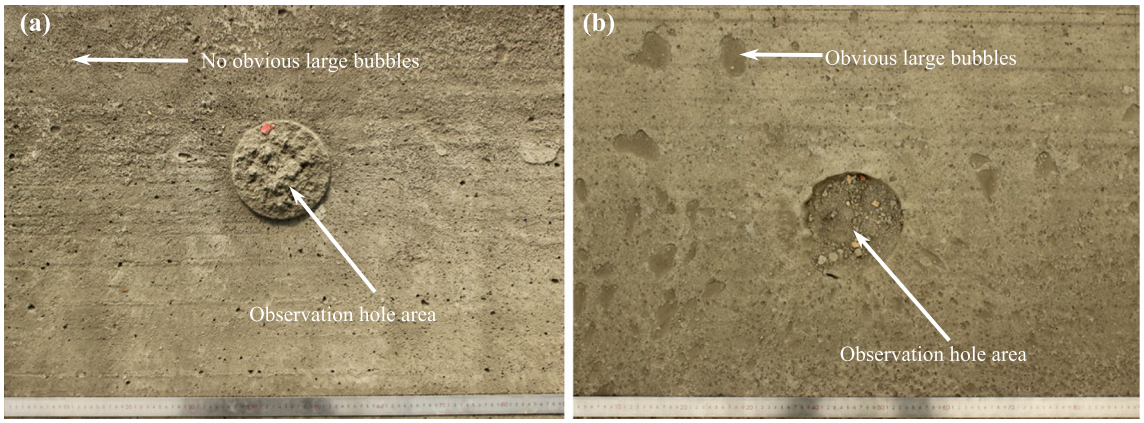

Fig. 10 Observation hole area: **a** the first plate; **b** the second plate

Table 2 The percent of each type of bubble defect area

Area	(10 mm^2, 100 mm^2) (%)	[100 mm^2, 600 mm^2) (%)	[600 mm^2, ∞) (%)
First plate	3.616	0.546	0.083
Second plate	4.977	5.950	6.343

Table 3 Classification of bubble defects (unit: mm^2)

No.	Area of defect	No	Area of defect
1	$100 < s < 200$	6	$600 \le s < 700$
2	$200 \le s < 300$	7	$700 \le s < 800$
3	$300 \le s < 400$	8	$800 \le s < 900$
4	$400 \le s < 500$	9	$900 \le s < 1000$
5	$500 \le s < 600$	10	$1000 \le s$

exceeding 1000 mm^2, although their occurrence probability was relatively low, their impact was significant when they did occur. The percentage of the cumulative area of each area with bubble defects of 1000 mm^2 or more relative to the bonding interface was substantial, ultimately resulting in a value below 0.8 MPa. The correlation between the bubble defect area, the percentage of the cumulative bubble defect area, and the relative rate of decrease in the splitting tensile strength value, as classified in Table 3, is presented in Table 4. It was observed that the decrease rate of the splitting tensile strength value was significantly enhanced as the percent of bubble defects increased.

To adhere to the design concept of this track structure, it was essential to establish a strong bonding interface that prevented any debonding occurrences. The bonding interface needed to counteract the adverse effects of bubble defects, which could reduce interfacial bonding strength, thereby ensuring long-term durability. Through the study of the impact of bubble defects, the correlation between the percent of the cumulative area of all bubble defects, and the splitting tensile strength value, is illustrated in Fig. 12.

It was observed that when the percentage reached 12%, the splitting tensile strength value was 0.67 MPa, exceeding the 0.5 MPa threshold, thereby ensuring that the interface did not debond. Similarly, when the percentage reached 8%, the value was 0.85 MPa, surpassing the 0.8 MPa threshold. This effectively mitigated the adverse effect of each area with bubble defects of 1000 mm^2 or more.

In conjunction with the study of the effect of interfacial defects on the rate of decrease in bonding strength in Fig. 11, the correlation between the percent of accumulation area of each area of 600 mm^2 or more bubble defect, and the relative decline rate of the splitting tensile strength value was analyzed, as illustrated in Fig. 13.

By analyzing Fig. 13, the decrease rate of the splitting tensile strength value gradually increased with the increase of the percent of the accumulated bubble defect area. When the percent was about 2%, a specimen with the splitting tensile strength value equal to 0.67 MPa appeared. When the percent was about 6%, a specimen with the splitting tensile strength value equal to 0.65 MPa occurred. When the percent was about 11.5%, a specimen with the splitting tensile strength value equal to 0.57 MPa appeared. According to the impact of the cumulative area percentage of all bubble defects on the strength value [70], maintaining a splitting tensile strength value greater than 0.5 MPa ensured the prevention of interface debonding, and the splitting tensile strength value was greater than 0.8 MPa that it could overcome the adverse effect of each area of 1000 mm^2 or more bubble defect. But when the percent of accumulation area of each area of 600 mm^2 or more bubble defect was 6%, the splitting tensile strength value decreased to below 0.8 MPa. In order to ensure sufficient bonding strength and to reduce the occurrence of specimens with lower splitting tensile strength value, the percent should be less than 6%.

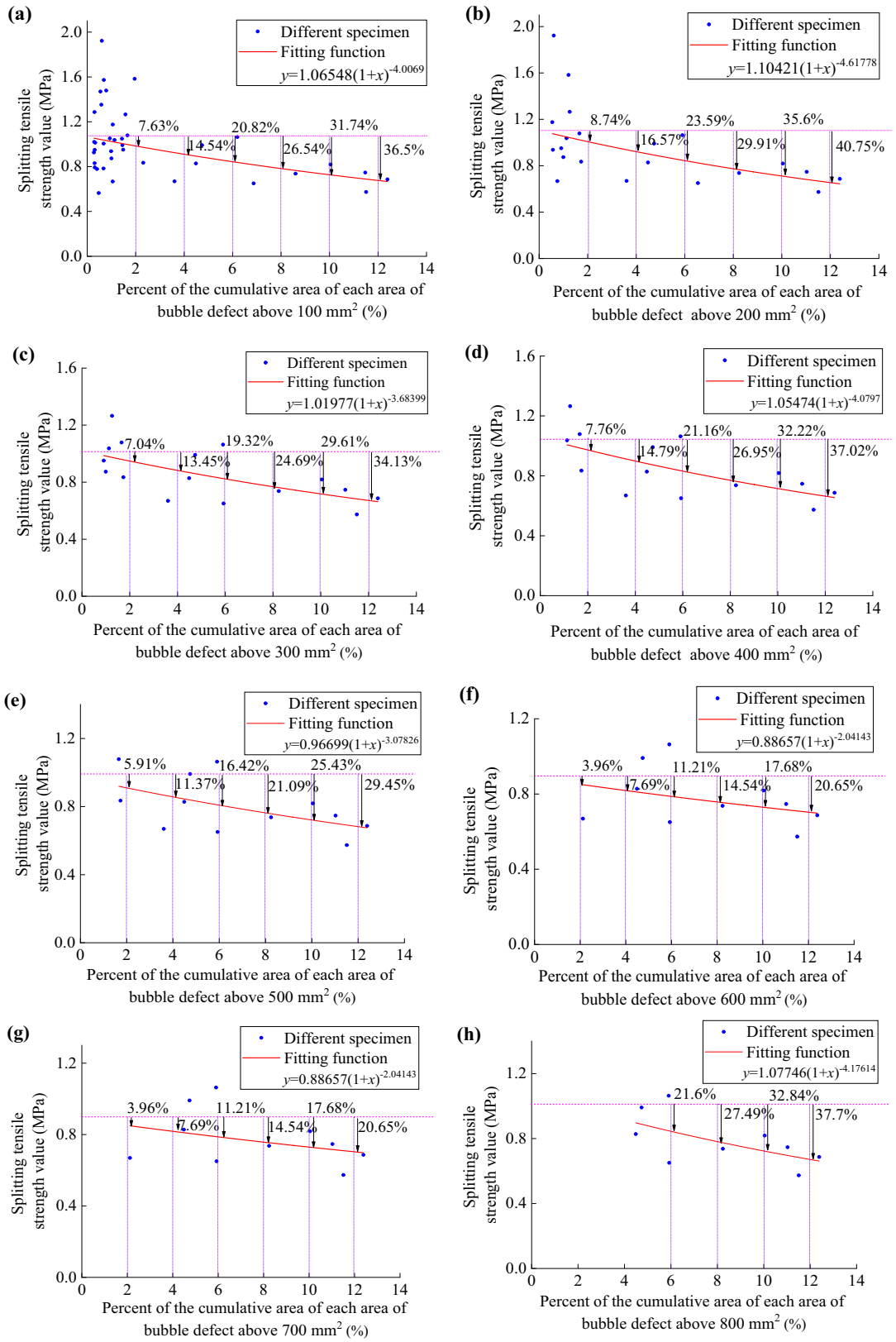

Fig. 11 The correlation between the classification of bubble defects, the percentage of the cumulative bubble defect area, and the relative rate of decrease in the splitting tensile strength value under different bubble defect areas: **a** above 100 mm^2; **b** above 200 mm^2; **c** above 300 mm^2; **d** above 400 mm^2; **e** above 500 mm^2; **f** above 600 mm^2; **g** above 700 mm^2; **h** above 800 mm^2; **i** above 900 mm^2; **j** above 1000 mm^2

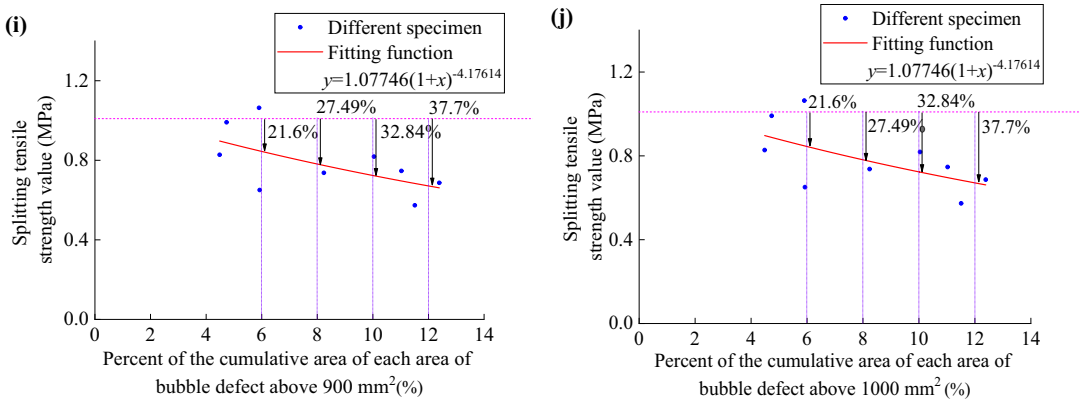

Fig. 11 (continued)

Table 4 The correlation between the bubble defect area, the percentage of the cumulative bubble defect area, and the relative rate of decrease in the splitting tensile strength value

Area of defects	Relative rate of decrease in splitting tensile strength (%)					
	Defects at 2%	Defects at 4%	Defects at 6%	Defects at 8%	Defects at 10%	Defects at 12%
Above 100 mm²	7.63	14.54	20.82	26.54	31.74	36.50
Above 200 mm²	8.74	**16.57**	23.59	29.91	35.60	40.75
Above 300 mm²	7.04	13.45	19.32	24.69	29.61	34.13
Above 400 mm²	7.76	14.79	21.16	26.95	32.22	37.02
Above 500 mm²	5.91	11.37	16.42	21.09	25.43	29.45
Above 600 mm²	3.96	7.69	11.21	14.54	17.68	20.65
Above 700 mm²	3.96	7.69	11.21	14.54	17.68	20.65
Above 800 mm²	–	–	21.60	27.49	32.84	37.70
Above 900 mm²	–	–	21.60	27.49	32.84	37.70
Above 1000 mm²	–	–	21.60	27.49	32.84	37.70

16.57% means that the relative decrease in the splitting tensile strength was 16.57%, when the percent of the accumulation of each area of 200 mm² or more bubble defects to the bonding interface reached 4%

4 Conclusions

In this study, the authors proposed utilizing the splitting tensile strength as an assessment method for evaluating the impact of bubble defects on interfacial bonding performance. The following conclusions were derived:

1. The SCC specimens were perfused using a consistent field perfusion process. For the majority of the specimens, the percentage of the total filling layer occupied by bubble defects, each with an area of 6 cm² or more, was zero. However, in a minority of specimens, this percentage exceeded 2%, and in some cases, it was significantly larger, reaching values of over 12%.
2. By analyzing bubble defects in two standard-sized filling layers, bubble defects with each area of 1 cm² or more

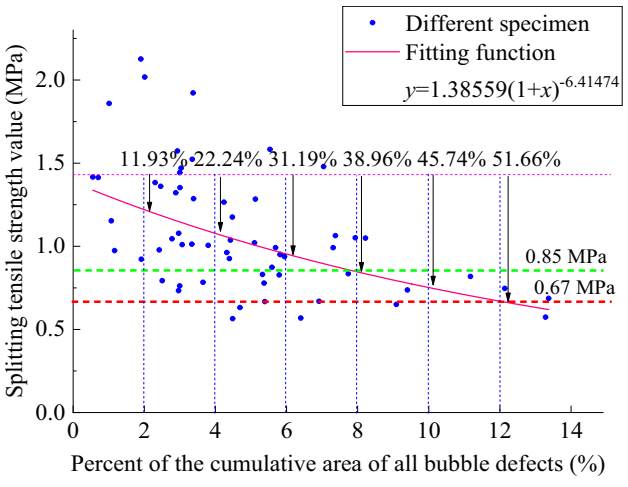

Fig. 12 The correlation between the percent of the cumulative area of all bubble defects and the strength value

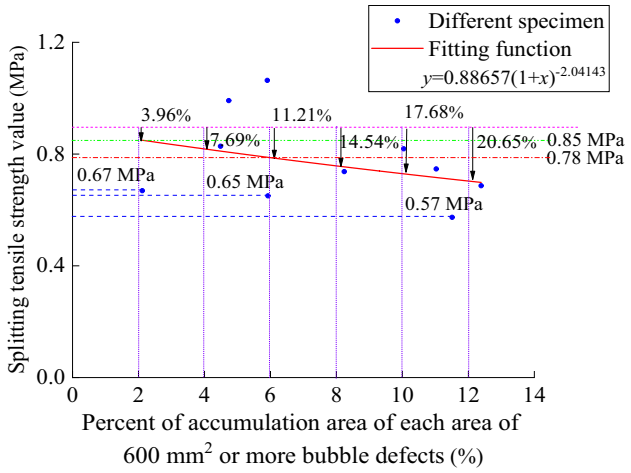

Fig. 13 The correlation between the percent of accumulation area of each area of 600 mm^2 or more bubble defect and the relative decline rate of the strength value

were classified and refined. The trend of each area of 1 cm^2 or more bubble defect was that the probability of occurrence decreased as single bubble defect increased. When it came to bubble defects with single defect area exceeding 10 cm^2, although the probability of their occurrence was relatively low. Once it did appear, the percent of the cumulative area of each area of 10 cm^2 or more bubble defect to the bonding interface was significant. This ultimately resulted in a lower value and was below 0.8 MPa.

3. The correlation study was conducted to investigate the relationship between the percent of the cumulative area of all bubble defects and the splitting tensile strength value. When the percent was equal to 12%, the splitting tensile strength value was 0.67 MPa, which was greater than 0.5 MPa, so as to ensure that the interface was not debonded. When the percent was equal to 8%, the value was 0.85 MPa. It was greater than 0.8 MPa, thus overcoming the adverse effect of each area of 10 cm^2 or more bubble defect.
4. The study aimed to investigate the correlation between the percentage of the cumulative area occupied by bubble defects, each with an area of 6 cm^2 or more, and the relative decrease in the splitting tensile strength value. Specifically, when this percentage was approximately 2%, the specimen exhibiting a splitting tensile strength of 0.67 MPa was observed. As the percentage increased to around 6%, the specimen with a splitting tensile strength of 0.65 MPa was noted. Furthermore, when the percentage reached about 11.5%, the specimen with a splitting tensile strength of 0.57 MPa was identified. To maintain adequate bonding strength and minimize the occurrence of specimens with reduced splitting tensile strength, it was recommended that the percentage should not exceed 6%.

Acknowledgements The work described in this paper was supported by a grant from China railway corporation science and technology research and development plan project (Grant No. 2017G005-B). The authors would like to appreciate the funding support by Wuyi University's Hong Kong and Macao Joint Research and Development Fund (Grants No. 2021WGALH15). The authors would also like to appreciate the funding support by the Innovation and Technology Commission of Hong Kong SAR Government to the Hong Kong Branch of National Rail Transit Electrification and Automation Engineering Technology Research Center (Grant No. K-BBY1).

References

1. Long G, Liu H, Ma K et al (2018) Development of high-performance self-compacting concrete applied as the filling layer of high-speed railway. J Mater Civ Eng 30(2):04017268
2. Sari M, Prat E, Labastire JF (1999) High strength self-compacting concrete original solutions associating organic and inorganic admixtures. Cem Concr Res 29(6):813818
3. Domone PL (2006) Self-compacting concrete: an analysis of 11 years of case studies. Cem Concr Compos 28(2):197–208
4. Brouwers HJH, Radix HJ (2005) Self-compacting concrete: theoretical and experimental study. Cem Concr Res 35(11):2116–2136
5. Okamura H, Ouchi M (1998) Self-compacting high performance concrete. Prog Struct Mater Eng 1(4):378–383
6. Aslani F, Nejadi S (2013) Self-compacting concrete incorporating steel and polypropylene fibers: compressive and tensile strengths, moduli of elasticity and rupture, compressive stress–strain curve, and energy dissipated under compression. Compos Part B Eng 53:121–133
7. National Railway Administration of the People's Republic of China (2018) Standard for acceptance of track works in high-speed railway. TB 10754–2018. China Railway Publishing House, Beijing
8. China Railway (2017) Specification of self-compacting concrete for high-speed railway CRTS III slab ballastless track. Q/CR 596–2017. China Railway Publishing House, Beijing
9. Yan W, Cui W, Qi L (2020) Effect of aggregate gradation and mortar rheology on static segregation of self-compacting concrete. Constr Build Mater 259:119816
10. Malazdrewicz S, Adam Ostrowski K, Sadowski Ł (2023) Self-compacting concrete with recycled coarse aggregates from concrete construction and demolition waste—current state-of-the art and perspectives. Constr Build Mater 370:130702

11. Kumar P, Pasla D, Jothi Saravanan T (2023) Self-compacting lightweight aggregate concrete and its properties: a review. Constr Build Mater 375:130861
12. Zhang H, Zhang J, Yang Y et al (2021) Effects of asphalt emulsion on the durability of self-compacting concrete. Constr Build Mater 292:123322
13. Liu H, Duan G, Wang F et al (2022) Investigation on mechanical behaviors of self-compacting concrete containing reclaimed asphalt pavement. Constr Build Mater 346:128421
14. Ansari rad T, Tanzadeh J, Pourdada A, (2020) Laboratory evaluation of self-compacting fiber-reinforced concrete modified with hybrid of nanomaterials. Constr Build Mater 232:117211
15. Gao Y, Zhou W, Zeng W et al (2021) Preparation and flexural fatigue resistance of self-compacting road concrete incorporating nano-silica particles. Constr Build Mater 278:122380
16. Quercia G, Spiesz P, Hüsken G et al (2014) SCC modification by use of amorphous nano-silica. Cem Concr Compos 45:69–81
17. Song Q, Yu R, Wang X et al (2018) A novel self-compacting ultra-high performance fibre reinforced concrete (SCUHPFRC) derived from compounded high-active powders. Constr Build Mater 158:883–893
18. Chen J, Zhuang J, Shen S et al (2022) Experimental investigation on the impact resistance of rubber self-compacting concrete. Structures 39:691–704
19. Chen X, Liu Z, Guo S et al (2019) Experimental study on fatigue properties of normal and rubberized self-compacting concrete under bending. Constr Build Mater 205:10–20
20. Li N, Long G, Ma C et al (2019) Properties of self-compacting concrete (SCC) with recycled tire rubber aggregate: a comprehensive study. J Clean Prod 236:117707
21. Bignozzi MC, Sandrolini F (2006) Tyre rubber waste recycling in self-compacting concrete. Cem Concr Res 36(4):735–739
22. Ferrara L, Park YD, Shah SP (2007) A method for mix-design of fiber-reinforced self-compacting concrete. Cem Concr Res 37(6):957–971
23. De La Rosa Á, Ortega JJ, Ruiz G et al (2023) Autogenous self-healing induced by compressive fatigue in self-compacting steel-fiber reinforced concrete. Cem Concr Res 173:107278
24. Corinaldesi V, Moriconi G (2004) Durable fiber reinforced self-compacting concrete. Cem Concr Res 34(2):249–254
25. Algin Z, Ozen M (2018) The properties of chopped basalt fibre reinforced self-compacting concrete. Constr Build Mater 186:678–685
26. Samimi K, Kamali-Bernard S, Maghsoudi AA (2018) Durability of self-compacting concrete containing pumice and zeolite against acid attack, carbonation and marine environment. Constr Build Mater 165:247–263
27. He J, Zhu M, Sang G et al (2023) Effect of PVA latex powder and PP fiber on property of self-compacting alkali-activated slag repair mortar. Constr Build Mater 408:133703
28. Mousavi SR, Afshoon I, Bayatpour MA et al (2021) Effect of waste glass and curing aging on fracture toughness of self-compacting mortars using ENDB specimen. Constr Build Mater 282:122711
29. Zhu W, Gibbs JC (2005) Use of different limestone and chalk powders in self-compacting concrete. Cem Concr Res 35(8):1457–1462
30. Ye G, Liu X, De Schutter G et al (2007) Influence of limestone powder used as filler in SCC on hydration and microstructure of cement pastes. Cement Concr Compos 29(2):94–102
31. Cunha VMCF, Barros JAO, Sena-Cruz JM (2011) An integrated approach for modelling the tensile behaviour of steel fibre reinforced self-compacting concrete. Cem Concr Res 41(1):64–76
32. Frazão C, Barros J, Camões A et al (2016) Corrosion effects on pullout behavior of hooked steel fibers in self-compacting concrete. Cem Concr Res 79:112–122
33. Grünewald S, Walraven JC (2001) Parameter-study on the influence of steel fibers and coarse aggregate content on the fresh properties of self-compacting concrete. Cem Concr Res 31(12):1793–1798
34. Torrijos MC, Barragán BE, Zerbino RL (2008) Physical–mechanical properties, and mesostructure of plain and fibre reinforced self-compacting concrete. Constr Build Mater 22(8):1780–1788
35. Ghanbari A, Karihaloo BL (2009) Prediction of the plastic viscosity of self-compacting steel fibre reinforced concrete. Cem Concr Res 39(12):1209–1216
36. Abrishambaf A, Barros JAO, Cunha VMCF (2013) Relation between fibre distribution and post-cracking behaviour in steel fibre reinforced self-compacting concrete panels. Cem Concr Res 51:57–66
37. Deeb R, Karihaloo BL, Kulasegaram S (2014) Reorientation of short steel fibres during the flow of self-compacting concrete mix and determination of the fibre orientation factor. Cem Concr Res 56:112–120
38. Qiu L, Dong S, Yu X (2021) Self-sensing ultra-high performance concrete for in-situ monitoring. Sens Actuators A 331:113049
39. Abrishambaf A, Barros JAO, Cunha VMCF (2015) Time-dependent flexural behaviour of cracked steel fibre reinforced self-compacting concrete panels. Cem Concr Res 72:21–36
40. Łaźniewska-Piekarczyk B (2013) The frost resistance versus air voids parameters of high performance self compacting concrete modified by non-air-entrained admixtures. Constr Build Mater 48:1209–1220
41. Kanagaraj B, Anand N, Diana Andrushia A (2023) Pull-out behavior and microstructure characteristics of binary blended self-compacting geopolymer concrete subjected to elevated temperature. Alex Eng J 76:469–490
42. Kamseu E, Ponzoni C, Tippayasam C et al (2016) Self-compacting geopolymer concretes: effects of addition of aluminosilicate-rich fines. J Build Eng 5:211–221
43. Xie Y, Liu B, Yin J (2002) Optimum mix parameters of high-strength self-compacting concrete with ultrapulverized fly ash. Cem Concr Res 32(3):477–480
44. Djelal C, Vanhove Y, Magnin A (2004) Tribological behaviour of self compacting concrete. Cem Concr Res 34(5):821–828
45. Pan C, Jin F, Zhou H (2022) Early-age performance of self-compacting concrete under stepwise increasing compression. Cem Concr Res 162:107002
46. Reinhardt H-W, Stegmaier M (2006) Influence of heat curing on the pore structure and compressive strength of self-compacting concrete (SCC). Cem Concr Res 36(5):879–885
47. Bao J, Zheng R, Zhang P (2023) Thermal resistance, water absorption and microstructure of high-strength self-compacting lightweight aggregate concrete (HSSC-LWAC) after exposure to elevated temperatures. Constr Build Mater 365:130071
48. Craeye B, De Schutter G, Desmet B et al (2010) Effect of mineral filler type on autogenous shrinkage of self-compacting concrete. Cem Concr Res 40(6):908–913
49. Valcuende M, Marco E, Parra C et al (2012) Influence of limestone filler and viscosity-modifying admixture on the shrinkage of self-compacting concrete. Cem Concr Res 42(4):583–592
50. Feys D, Verhoeven R, De Schutter G (2008) Fresh self compacting concrete, a shear thickening material. Cem Concr Res 38(7):920–929
51. Schwartzentruber LDA, Le Roy R, Cordin J (2006) Rheological behaviour of fresh cement pastes formulated from a self compacting concrete (SCC). Cem Concr Res 36(7):1203–1213
52. Geiker MR, Brandl M, Thrane LN et al (2002) The effect of measuring procedure on the apparent rheological properties of self-compacting concrete. Cem Concr Res 32(11):1791–1795

53. Feys D, Verhoeven R, De Schutter G (2009) Why is fresh self-compacting concrete shear thickening? Cem Concr Res 39(6):510–523
54. Belmonte IM, Benito Saorin FJ, Costa CP et al (2020) Quality of the surface finish of self-compacting concrete. J Build Eng 28:101068
55. Wang X, Liang J, Ren J et al (2023) Constitutive relations, mechanical behaviour, and failure criterion of microcapsule-based self-healing concrete under uniaxial and triaxial compression. J Build Eng 65:105773
56. Liu H, Duan G, Wang F et al (2023) Numerical simulation of effect of reclaimed asphalt pavement on damage evolution behavior of self-compacting concrete under compressive loading. Constr Build Mater 395:132323
57. Alyhya WS, Kulasegaram S, Karihaloo BL (2017) Simulation of the flow of self-compacting concrete in the V-funnel by SPH. Cem Concr Res 100:47–59
58. Kanellopoulos A, Savva P, Petrou MF et al (2020) Assessing the quality of concrete-reinforcement interface in self compacting concrete. Constr Build Mater 240:117933
59. Kaffetzakis MI, Papanicolaou CG (2016) Bond behavior of reinforcement in lightweight aggregate self-compacting concrete. Constr Build Mater 113:641–652
60. Lu Y, Liu Z, Li S et al (2018) Bond behavior of steel fibers reinforced self-stressing and self-compacting concrete filled steel tube columns. Constr Build Mater 158:894–909
61. Lu Y, Liu Z, Li S et al (2018) Bond behavior of steel-fiber-reinforced self-stressing and self-compacting concrete-filled steel tube columns for a period of 2.5 years. Constr Build Mater 167:33–43
62. Figueiras H, Nunes S, Coutinho JS et al (2009) Combined effect of two sustainable technologies: Self-compacting concrete (SCC) and controlled permeability formwork (CPF). Constr Build Mater 23(7):2518–2526
63. Dybeł P (2021) Effect of bottom-up placing of self-compacting concrete on microstructure of rebar-concrete interface. Constr Build Mater 299:124359
64. Wu L, Xu X, Wang H et al (2022) Experimental study on bond properties between GFRP bars and self-compacting concrete. Constr Build Mater 320:126186
65. Choi YW, Kim YJ, Shin HC et al (2006) An experimental research on the fluidity and mechanical properties of high-strength lightweight self-compacting concrete. Cem Concr Res 36(9):1595–1602
66. Xie Y, Corr DJ, Chaouche M et al (2014) Experimental study of filling capacity of self-compacting concrete and its influence on the properties of rock-filled concrete. Cem Concr Res 56:121–128
67. Ministry of Housing and Urban-Rural Development of the People's Republic of China (2019) Standard for test methods of concrete physical and mechanical properties. GB/T 50081-2019. China Architecture & Building Press, Beijing
68. Guan J, Hu X, Xie C et al (2018) Wedge-splitting tests for tensile strength and fracture toughness of concrete. Theor Appl Fract Mech 93:263–275
69. Randl N, Steiner M, Peyerl M (2020) Hochfester aufbeton zur tragwerksverstärkung. Beton Und Stahlbetonbau 115(2):106–116
70. Jiang W, Xie Y, Li W (2021) Influence of bubble defects on the bonding performance of the interlayer interface of the CRTS III slab ballastless track structure. Constr Build Mater 307:125003